

## Chapter 1

# SEARCHING FOR DOUBLE BETA DECAY TO EXCITED STATES

## 1.1 Introduction

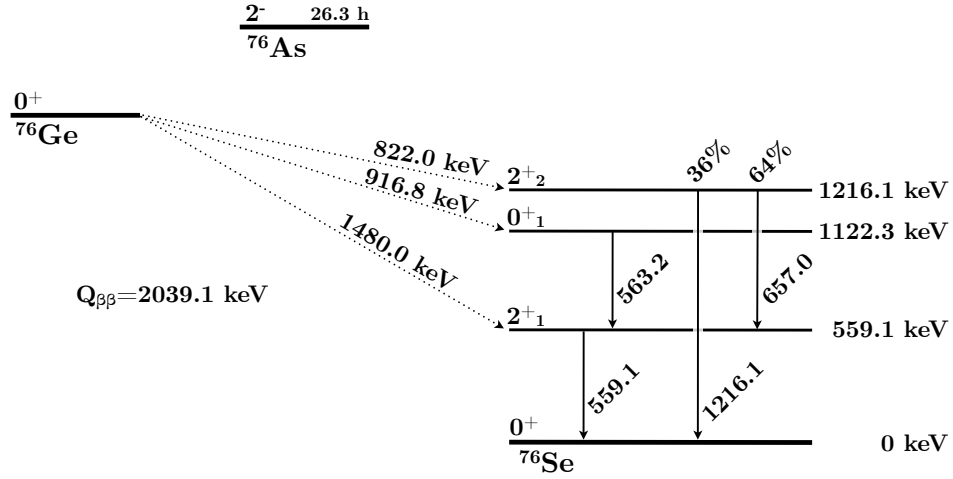


Figure 1.1: Energy level diagram for  $\beta\beta$ -decay of  $^{76}\text{Ge}$  to  $^{76}\text{Se}$ , including excited states. The  $Q$ -values for each decay branch and the energies and branching ratios for the deexcitation  $\gamma$ s are shown next to their corresponding lines.

$^{76}\text{Se}$  has 3 excited states that  $^{76}\text{Ge}$  can decay into in addition to the ground state, as shown in Figure 1.9. While the ground state decay has been observed, none of the decays to excited states have been yet; current experimental limits and theoretical estimates for the half-life of each decay are listed in Table ???. Each excited state decay will have a  $\beta\beta$ -decay with a reduced  $Q$ -value compared to the ground state decay. The excited state decays will also promptly produce one or two  $\gamma$ -rays at known energies. These  $\gamma$ s will typically

travel several cm before absorption and will often hit a different detector from the  $\beta\beta$ -decay site, meaning that we can search for peaks at these energies. Furthermore, since these  $\gamma$  events must hit a separate detector from the site of the  $\beta\beta$ -decay, the events containing this peak are inherently multi-detector. As shown in Figure 1.2, by searching for the peak only in events with high hit multiplicity, i.e. events that involve 2 or more detectors hit,  $\sim 85\%$  of backgrounds can be cut, while only sacrificing  $\sim 25\%$  of the signal. Additionally, the coincident detector hit(s) can provide additional observables that can be used to further discriminate excited state signals from multi-site backgrounds. This chapter will describe the various background reduction data cuts and how they are implemented. It will also evaluate the detection efficiency and systematic error associated with each cut based on simulations of the MAJORANA DEMONSTRATOR. The analysis presented in this chapter applies to the  $2\nu\beta\beta$ -decay to the  $0_1^+$  state of  $^{76}\text{Se}$ , which has  $Q_{\beta\beta} = 916.8$  keV and emits two  $\gamma$ s at 559.1 keV and 563.2 keV. The same analysis is applied to all other excited states in both the  $0\nu\beta\beta$  and  $2\nu\beta\beta$  decay modes, and the results are presented in Appendix ??.

## 1.2 Selection of Multi-Detector Events

Simultaneous detector hits are combined into events by the event builder (see Section ?? and Appendix ??). Events are combined in a  $4 \mu\text{s}$  rolling window. This window is expected to accept virtually all true coincidence events (see Figure 1.3). In a small number of runs, clocks between different Gretina cards were desynchronized. For these runs, the clocks were resynchronized by applying a timing offset during event building that is measured by seeking the time offset that aligns pulser events. With a typical overall rate between both modules of  $< 1$  Hz,  $< 0.4\%$  of all multi-site events are expected to originate from accidental coincidences, making this a negligible background. Once all the data has gone through the processing chain described in Section ??, the skim files from all good open runs in datasets 16a are collected into a single skim file containing a **TTree** with only multi-site events by the program `es.skimdata`.

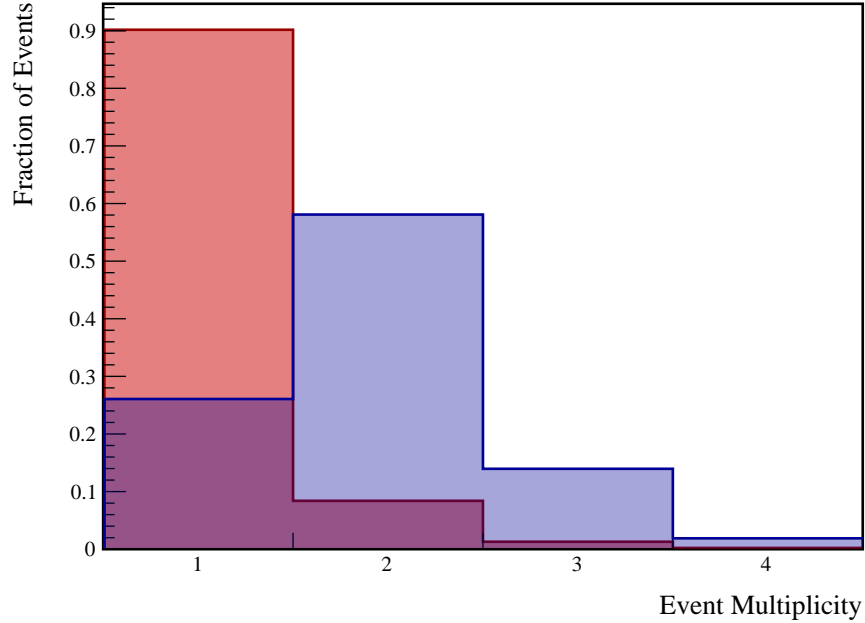


Figure 1.2: The simulated distribution of ROI event multiplicities in the background model and  $\beta\beta$  E.S. to  $0_1^+$  decay in DS6.

### 1.2.1 Variation in Detector Configuration

Throughout the runtime of the MAJORANA DEMONSTRATOR, not all detectors were simultaneously active, and within each dataset, the set of active detectors varied significantly. Because we are looking at multi-site event events, the detection efficiency for  $\beta\beta$  E.S. events in any detector depends on which other detectors are enabled. For this reason, detection efficiency is computed for each module in its entirety rather than for individual detectors. To account for changes in detector configuration, each dataset is divided into subdatasets based on which detectors are active. The subdatasets are described by a pair of 64-bit masks, one for each module, with each bit representing a single detector's state. To decode the bitmask,

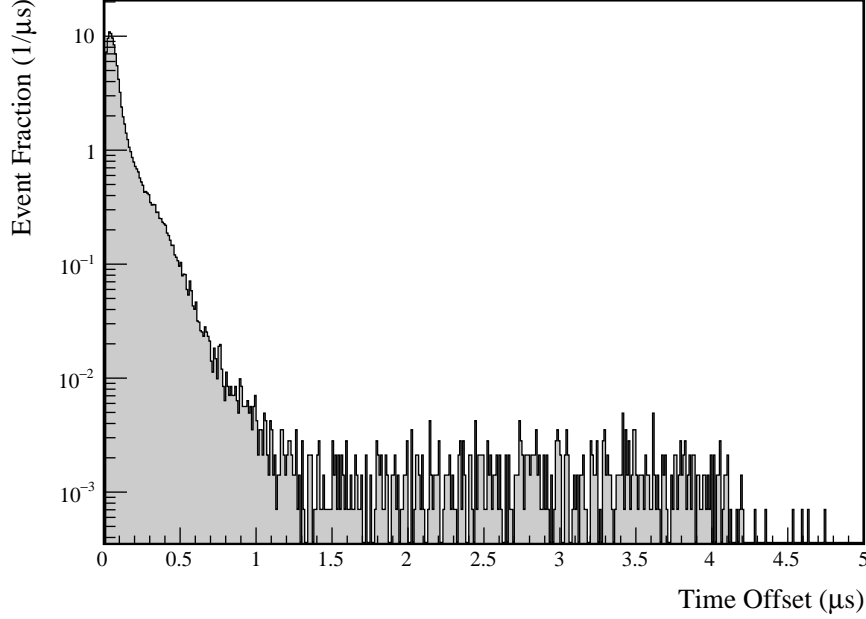


Figure 1.3: Distribution of time interval between individual hits within a multi-detector event during a  $^{228}\text{Th}$  calibration run. Offsets of greater than  $\sim 1.5 \mu\text{s}$  are due to pileup, which is significant due to the high data rate of calibration runs. Offsets greater than  $\sim 4 \mu\text{s}$  must involve events with more than two hits, due to the event builder time window.

the  $b$ 'th least significant bit represents string position  $P$ , detector position  $D$  if

$$b = 8 \cdot P + D \quad (1.1)$$

The set of runs and active channels for each run were determined by the run selection and data cleaning committee, and the procedures are outlined in [4]. The program `es_getdatasets` uses these selections to sort each run into a subdataset.

The detection efficiency is defined as the probability of a signal event in any detector, including inactive detectors. Detection efficiency is calculated individually for each subdataset and for each module by creating a separate skim file for each subdataset as outlined in Section ???. The final efficiency is then computed as an isotopic exposure weighted average of

the efficiency within each subdataset. Any efficiency uncertainties are assumed to be totally correlated between subdatasets. The livetime of each subdataset is calculated by the program `es_livetimes` by totalling the run time in each run, and subtracting any deadtime that affects the entire module, including deadtime caused by the muon veto system and by liquid nitrogen fills. Additional sources of deadtime that affect individual detectors are calculated as inefficiencies rather than being subtracted from the livetime, as discussed in Section ??.

This is done because deadtime in any individual detector affects the detection efficiency of all other detectors. The isotopic exposure is computed by multiplying the livetime of each module by the total isotopic mass in each module. Since this includes mass in inactive detectors and dead layers, the isotopic exposure for this analysis will differ from that presented in the  $0\nu\beta\beta$  analysis. Table 1.1 lists each subdataset along with its livetime and exposure.

DS	M1 Detector Mask	M2 Detector Mask	Run Time (days)	M1 L.T. (days)	M1 Eff.	M2 L.T. (days)	M2 Eff.	Exposure (kg.y)
DS1	061a08001e0e1c00	0000000000000000	2.64	2.60	1.693%	0.00	0.000%	0.109
DS1	161a08341e0e1c00	0000000000000000	0.02	0.02	1.978%	0.00	0.000%	0.001
DS1	161a0c341e0e1c00	0000000000000000	4.51	4.48	1.915%	0.00	0.000%	0.188
DS1	161a0c361e0e1c00	0000000000000000	3.49	3.48	1.449%	0.00	0.000%	0.146
DS1	1e1a00001e0e1c00	0000000000000000	7.82	7.73	2.015%	0.00	0.000%	0.324
DS1	1e1a08001e0e1c00	0000000000000000	25.49	25.19	2.202%	0.00	0.000%	1.057
DS1	1e1a08041e0e1c00	0000000000000000	2.95	2.93	2.277%	0.00	0.000%	0.123
DS1	1e1a08141e0e1c00	0000000000000000	0.26	0.25	2.297%	0.00	0.000%	0.011
DS1	1e1a08301e0e1c00	0000000000000000	1.40	1.37	2.305%	0.00	0.000%	0.057
DS1	1e1a08341e0e1c00	0000000000000000	7.58	7.50	2.095%	0.00	0.000%	0.315
DS1	1e1a0c001e0e1c00	0000000000000000	1.96	1.93	2.226%	0.00	0.000%	0.081
DS1	1e1a0c341e0e1c00	0000000000000000	0.67	0.67	2.296%	0.00	0.000%	0.028
DS2	1e1a08001e0e1c00	0000000000000000	9.58	9.51	2.248%	0.00	0.000%	0.399
DS3	1e1a0c3e1e0e1c00	0000000000000000	29.88	29.67	2.566%	0.00	0.000%	1.245
DS4	0000000000000000	1c061a16060e1e00	19.15	0.00	0.000%	18.85	1.811%	0.622
DS5a	08000020040e1c00	18060a02040e1e00	1.49	1.48	0.703%	1.46	1.111%	0.110
DS5a	08080020040e1c00	18060a16060e1e00	2.51	2.49	0.842%	2.47	1.484%	0.186
DS5a	08080030040e1c00	18060a02040e1e00	0.01	0.01	0.888%	0.01	1.094%	0.001
DS5a	0e1a04321e0e1c00	08020a16060e1e00	2.69	2.71	2.265%	2.66	1.165%	0.201
DS5a	0e1a0c321e0e1c00	0000000000000000	0.65	0.63	2.522%	0.00	0.000%	0.026
DS5a	0e1a0c321e0e1c00	08060a16060e1e00	1.24	1.24	2.513%	1.21	1.451%	0.092

*Continued on the next page*

Table 1.1: List of subdatasets

DS	M1 Detector Mask	M2 Detector Mask	Run Time (days)	M1 L.T. (days)	M1 Eff.	M2 L.T. (days)	M2 Eff.	Exposure (kg.y)
DS5a	0e1a0c321e0e1c00	18060a02040e1e00	2.94	2.92	2.288%	2.89	1.098%	0.218
DS5a	0e1a0c321e0e1c00	18060a1406061600	0.04	0.04	2.487%	0.04	0.906%	0.003
DS5a	0e1a0c321e0e1c00	18060a1606060600	3.19	3.15	2.452%	3.16	0.774%	0.237
DS5a	0e1a0c321e0e1c00	18060a16060e0600	3.30	3.28	2.458%	3.29	0.793%	0.246
DS5a	0e1a0c3e1e0e1c00	1806020606081800	1.75	1.73	2.703%	1.73	0.726%	0.129
DS5a	0e1a0c3e1e0e1c00	18060216060c1c00	6.84	6.77	2.698%	6.74	1.068%	0.507
DS5a	0e1a0c3e1e0e1c00	18060216060e1e00	13.48	13.30	2.677%	13.27	1.189%	0.996
DS5a	0e1a0c3e1e0e1c00	18060816060e1c00	0.05	0.05	2.502%	0.05	1.247%	0.004
DS5a	0e1a0c3e1e0e1c00	18060a0606060c00	2.16	2.12	2.670%	2.12	0.982%	0.159
DS5a	0e1a0c3e1e0e1c00	18060a16040e1e00	0.76	0.76	2.668%	0.74	1.222%	0.056
DS5a	0e1a0c3e1e0e1c00	18060a1606060c00	0.25	0.25	2.682%	0.25	1.060%	0.019
DS5a	0e1a0c3e1e0e1c00	18060a1606061800	1.88	1.86	2.686%	1.86	0.998%	0.140
DS5a	0e1a0c3e1e0e1c00	18060a1606061c00	9.20	9.13	2.657%	9.06	1.353%	0.682
DS5a	0e1a0c3e1e0e1c00	18060a16060c1c00	7.89	7.79	2.688%	7.79	1.350%	0.584
DS5a	0e1a0c3e1e0e1c00	18060a16060e1c00	11.68	11.53	2.340%	11.51	1.357%	0.864
DS5a	0e1a0c3e1e0e1c00	18060a16060e1e00	5.21	5.15	2.665%	5.13	1.486%	0.386
DS5a	0e1a0c3e1e0e1c00	18061216060e1e00	2.39	2.37	2.676%	2.37	1.266%	0.178
DS5b	1e1a0c3e1e0c1c00	18061216060e1e00	24.46	24.09	2.672%	24.06	1.268%	1.805
DS5b	1e1a0c3e1e0c1c00	18061a16060e1e00	0.75	0.75	2.670%	0.75	1.654%	0.056
DS5b	1e1a0c3e1e0e1c00	18061216060e1e00	14.28	14.12	2.766%	14.07	1.169%	1.057
DS5c	1e1a0c3e1e0c1c00	00060216060e0e00	0.00	0.00	2.567%	0.00	0.787%	0.000
DS5c	1e1a0c3e1e0c1c00	00060a16060e0e00	0.91	0.89	2.664%	0.91	1.016%	0.067
DS5c	1e1a0c3e1e0c1c00	00061216060e0e00	10.22	10.15	2.645%	10.03	0.857%	0.757
DS6a	12000000000c0800	1002020006040600	1.33	1.31	0.160%	1.31	0.230%	0.099
DS6a	12000c20000c1c00	18061216060c1600	6.93	6.84	0.756%	6.86	0.679%	0.514
DS6a	12020000040c0800	1802020006040600	1.30	1.28	0.284%	1.28	0.275%	0.096
DS6a	12020c00040c1800	1802020006040600	2.37	2.33	0.676%	2.33	0.275%	0.175
DS6a	12080c20000c1c00	18061216060c1600	3.38	3.34	0.931%	3.34	0.677%	0.251
DS6a	12120c3e1c0c1c00	18061216060c1600	0.56	0.54	1.847%	0.56	0.676%	0.041
DS6a	16020c10040c1800	1806020006060600	3.23	3.20	0.883%	3.19	0.416%	0.239
DS6a	160a0c321c0c1c00	1806021006061600	1.98	1.95	2.022%	1.97	0.521%	0.147
DS6a	1e0a0c321c0c1c00	1806020006040200	2.62	2.59	2.275%	2.59	0.260%	0.194
DS6a	1e0a0c321c0c1c00	1806020006040600	1.31	1.29	2.275%	1.29	0.390%	0.097
DS6a	1e0a0c321c0c1c00	1806020006041600	1.30	1.28	2.275%	1.26	0.459%	0.096
DS6a	1e0a0c321c0c1c00	1806021006061600	1.61	1.59	2.275%	1.59	0.521%	0.119
DS6a	1e120c3e1c0c1c00	18061216060c1600	0.95	0.93	2.284%	0.93	0.676%	0.070
DS6a	1e1a0c321c0c1c00	1806020006060600	1.30	1.28	2.457%	1.28	0.416%	0.096
DS6a	1e1a0c321c0c1c00	1806021006040600	3.91	3.88	2.457%	3.87	0.415%	0.291

Continued on the next page

Table 1.1: List of subdatasets

DS	M1 Detector Mask	M2 Detector Mask	Run Time (days)	M1 L.T. (days)	M1 Eff.	M2 L.T. (days)	M2 Eff.	Exposure (kg.y)
DS6a	1e1a0c321c0c1c00	1806021006041600	2.92	2.90	2.457%	2.90	0.495%	0.217
DS6a	1e1a0c321c0c1c00	1806021006060600	1.31	1.30	2.455%	1.30	0.436%	0.097
DS6a	1e1a0c3a1c0c1c00	1806020006040600	2.32	2.31	2.553%	2.32	0.390%	0.174
DS6a	1e1a0c3a1c0c1c00	1806021006040600	1.77	1.77	2.552%	1.75	0.415%	0.132
DS6a	1e1a0c3a1c0c1c00	1806021006041600	0.67	0.67	2.553%	0.67	0.494%	0.050
DS6a	1e1a0c3e1c0c1c00	1806000006040600	2.22	2.18	2.631%	2.16	0.360%	0.163
DS6a	1e1a0c3e1c0c1c00	1806020006041600	1.32	1.30	2.630%	1.30	0.458%	0.097
DS6a	1e1a0c3e1c0c1c00	1806021006041600	1.30	1.28	2.630%	1.28	0.494%	0.096
DS6a	1e1a0c3e1c0c1c00	18060210060c1600	4.63	4.58	2.629%	4.55	0.533%	0.342
DS6a	1e1a0c3e1c0c1c00	1806021206041600	2.61	2.56	2.628%	2.57	0.515%	0.192
DS6a	1e1a0c3e1c0c1c00	18060214060c0600	1.70	1.70	2.628%	1.68	0.492%	0.127
DS6a	1e1a0c3e1c0c1c00	18060214060c1600	1.38	1.36	2.627%	1.36	0.576%	0.102
DS6a	1e1a0c3e1c0c1c00	18060214060e1600	23.42	23.19	2.601%	23.12	0.555%	1.736
DS6a	1e1a0c3e1c0c1c00	18061212060c1600	2.93	2.89	2.628%	2.90	0.644%	0.217
DS6a	1e1a0c3e1c0c1c00	18061216060c1600	6.59	6.51	2.628%	6.51	0.690%	0.488
DSTotal	–	–	321.60	318.26	2.354%	238.53	0.987%	21.228

Table 1.1: List of each subdataset with its livetime, detection efficiency measured for the  $\beta\beta$  E.S.to  $0_1^+$  decay, and total isotopic exposure. Note the large variance in the detection efficiency.

### 1.2.2 Dead Layer Effects

For multi-detector events, each individual hit may be degraded by the deadlayer, so the loss of sensitivity from deadlayers is larger for this search than for searches for single-site events. For this reason, dead layer effects are treated as a loss of detection efficiency instead of a loss of exposure (as in the  $0\nu\beta\beta$  analysis). Dead layers are included in the simulations as a part of post-processing as described in Section ???. To account for uncertainty in the thickness of the deadlayer, two separate simulations are run, with and without deadlayers. By comparing the efficiency measurement from each simulation, we measure the size of the dead layer effect. The percent uncertainty in the efficiency loss from dead layers is assumed to be the same as the percent uncertainty in the dead layer thickness. Typical loss of efficiency for multi-site peaks is 25-35%; for the  $2\nu\beta\beta$  to the  $0_1^+$  decay, the losses are 26% for module 1 and 34% for

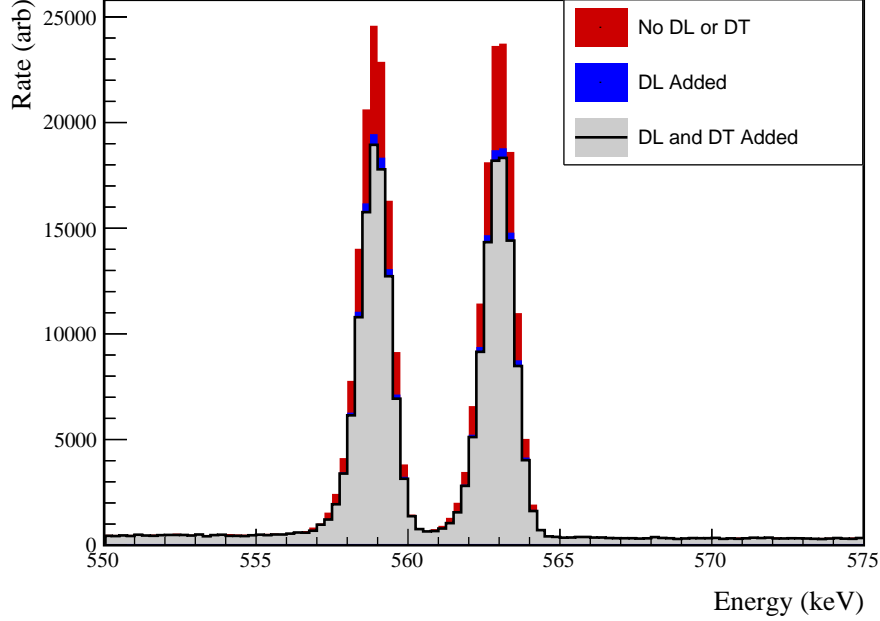


Figure 1.4: Effect of dead layers and dead times on peak amplitudes for  $2\nu\beta\beta$  to the  $0_1^+$  peaks in multi-site event events.

module 2. The uncertainty in the dead layer tends to be one of the dominant uncertainties in measuring the detection efficiency. This is much larger than the  $\sim 10\%$  loss seen in the  $0\nu\beta\beta$  analysis for two reasons. First, for multi-detector events, there are multiple hits that could possibly be lost to the dead layer. Second,  $\gamma$  hits will be more concentrated at the surface of the detectors, near the dead layers, than  $\beta\beta$  sites. The effect of dead layers on detection efficiency can be seen in Figure 1.4.

### 1.2.3 Dead Time Effects

Detector deadtimes, which affect only a single detector at a time, reduce the detection efficiency for events that occur in all detectors in the module. For this reason, instead of subtracting these deadtimes from the livetime, the deadtimes are incorporated into the



detection efficiency. Detector deadtimes are measured individually for each run by counting pulser events and comparing to the number of expected pulser events for each detector. The program `es_livetime` collects the detector deadtimes that are measured in this way and finds the average detector deadtime for each subdataset. These dead times are then applied to the simulation skimming process as described in Section ???. Similar to the dead layers, simulation files are produced with and without deadtimes in order to measure the size of the effect. Uncertainties in the detector deadtimes are measured as the statistical uncertainties from pulser counts. The percent uncertainty in efficiency loss from detector dead times is assumed to be the same as the average percent uncertainty in the detector dead time. Typical loss of efficiency from detector deadtimes range from 1-3%. For the  $2\nu\beta\beta$  to the  $0_1^+$  decay, the losses are 2.5% for module 1 and 1.9% for module 2. The effects of detector deadtimes can be seen in Figure 1.4.

#### 1.2.4 Simulation Validation and Errors

In addition to dead layer and dead time effects that can be explicitly accounted for, other possible sources of systematic uncertainty from the simulation exist, such as inaccuracies in the simulation geometry. To account for these, we use pair production events from calibration runs as a proxy for  $\beta\beta$  E.S. events. In pair production events, an electron-positron pair is produced in the bulk of a detector, followed promptly by two 511 keV  $\gamma$ s from the annihilation of the positron. Because these events involve a single pair production site and the prompt emission of gamma rays which may be absorbed in a separate detector, they make a good proxy for  $\beta\beta$  E.S. events. In single-escape peak (SEP) events, one gamma is absorbed in the detector containing the pair-production, while the other escapes, resulting in a source detector hit with energy equal to the  $\gamma$  energy minus 511 keV. In double-escape peak (DEP) events, both gammas escape the detector, resulting in a source detector hit with energy equal to the  $\gamma$  energy minus 1022 keV. Both both SEP and DEP events present the possibility for a second 511 keV detector hit. By comparing the rate of multiplicity-1 events in the SEPs and DEPs to the rate of multiplicity-2 events in which one hit falls into one of these peaks and

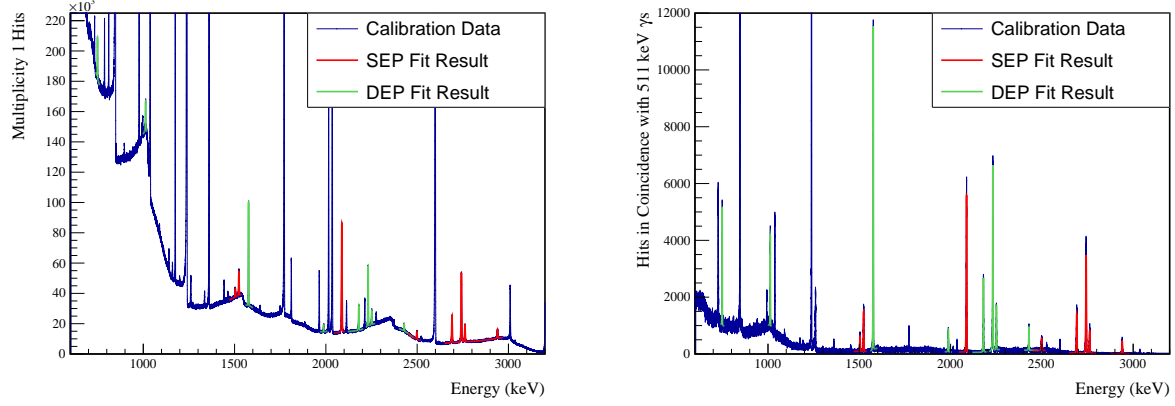


Figure 1.5: Spectra of multiplicity 1  $^{56}\text{Co}$  events (left) and multiplicity 2  $^{56}\text{Co}$  events in coincidence with an annihilation gamma. The results of the simultaneous peak fits are drawn in red (SEP fit) and green (DEP fit).

the other falls into the 511 keV peak, we can measure a proxy for the detection efficiency of our multi-site event signature. By comparing this measurement to simulation, we can estimate the size of any unknown uncertainties in our simulation-based efficiency estimate.

To achieve this, we will use a  $^{56}\text{Co}$  calibration source.  $^{56}\text{Co}$  presents the advantage of a large number of  $\gamma$ s at energies high enough to cause pair production, which allows for a comparison of many peaks to our simulation. A  $^{56}\text{Co}$  line source was inserted into the module 1 calibration track on January 15, 2019 and 168.1 hrs of data were recorded, until January 22, 2019. Immediately after this, the source was inserted into the module 2 calibration track and 167.1 hrs of data were recorded until January 29, 2019. The source had a nominal activity of 6 kHz, resulting in a high enough data rate that the energy threshold for each channel was raised to  $\sim 400$  keV. As discussed in Section ??, 3 billion event primaries were simulated for the  $^{56}\text{Co}$  source in each module's source track in order to achieve similar events statistics for both the simulations and data. Simulations were run with and without dead-layers.

8 SEPs and 7 DEPs were selected as proxies for the  $\beta\beta$  E.S. signal; these peaks were selected because of their prominence above the Compton continuum and the absence of nearby peaks that would interfere with a peak-height measurement. A simultaneous fit, as described in Appendix ??, of all SEPs as single-detector events and as two-detector events in coincidence with a 511 keV peak event was performed in the calibration data and in the simulations both with and without dead layers. SEPs and DEPs have abnormal peakshapes due to in-flight annihilation of the positrons, which results in Doppler broadening of the peak shapes. For this reason, a high energy tail is added to the typical peak shape function. The peak height ratios and uncertainties for peak  $k$  are determined as follows:

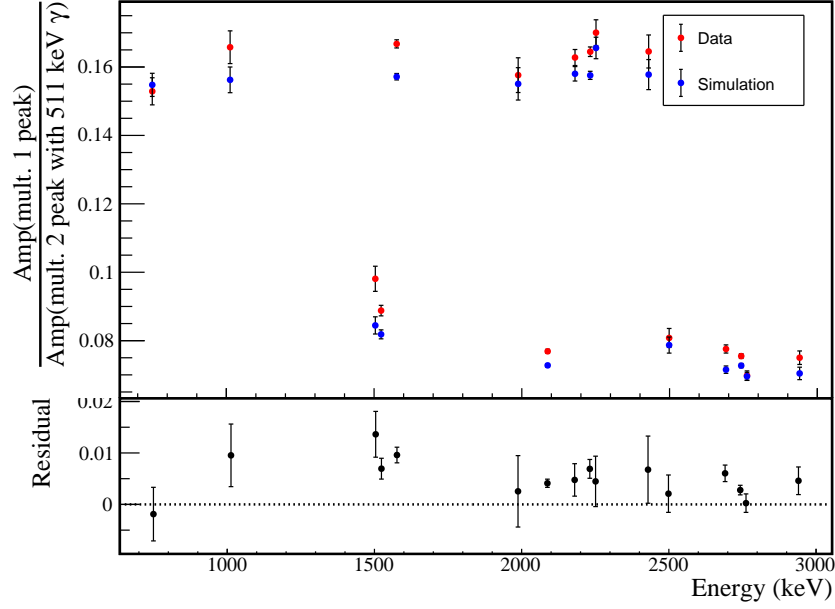
$$\epsilon_k = \frac{A_{k,m2}}{A_{k,m1}} \quad (1.2)$$

$$\sigma_{stat,k} = \epsilon_k \sqrt{\frac{\Sigma_{A,k,m1;A,k,m1}}{A_{k,m1}^2} - 2\frac{\Sigma_{A,k,m1;A,k,m2}}{A_{k,m1}A_{k,m2}} + \frac{\Sigma_{A,k,m2;A,k,m2}}{A_{k,m2}^2}} \quad (1.3)$$

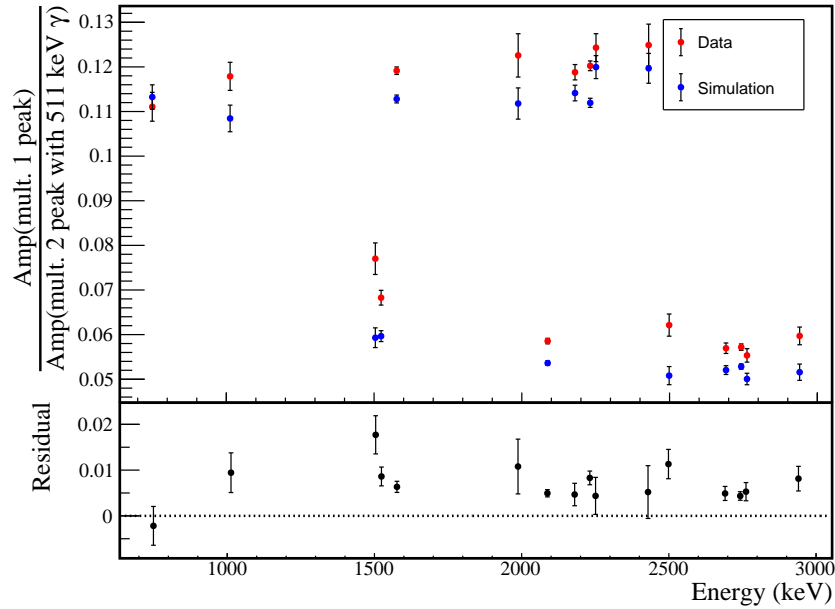
where  $A_{k,m1/2}$  are the fitted amplitudes of peak  $k$  with multiplicity 1 and multiplicity 2 respectively, and  $\Sigma_{A,k,m1/2;A,k,m1/2}$  is the fitter covariance matrix element for these amplitudes. The same process of simultaneously fitting DEPs is followed to extract the DEP peak-height ratios. The measured data spectra and fit results are shown in Figure 1.5.

Figure 1.6 shows an overall offset that cannot be explained by statistical errors; this discrepancy is measured and treated as a systematic error which will be applied to the  $\beta\beta$  E.S. measurement. Since some of this discrepancy can be explained by the dead layer uncertainty, the difference between the simulated peak-height ratios with and without the dead layer is multiplied by the percent uncertainty in the dead layer thickness in order to measure the systematic error caused by the dead layer. Finally, a  $\chi^2$  value is computed for the comparison between the simulated and measured peak-heights using the statistical and dead-layer uncertainties.

$$\chi^2(\mu, \delta_{DL}) = \sum_{k=1}^N \frac{(\epsilon_{k,meas} - \epsilon_{k,sim} - \delta_{DL} \cdot \sigma_{DL,k} - \mu)^2}{\sigma_{stat,dat,k}^2 + \sigma_{stat,sim,k}^2} + \delta_{DL}^2 \quad (1.4)$$



(a) Module 1



(b) Module 2

Figure 1.6: Measurement of peak height ratios between multiplicity 1 events and multiplicity 2 events containing a 511 keV annihilation  $\gamma$  for both simulated and measured  $^{56}\text{Co}$  spectra. Only statistical error bars are drawn. These ratios are listed in tables 1.2 and 1.3.

where  $\sigma_{DL,k}$  is the uncertainty from dead layers,  $\delta_{DL}$  is the measured error from deadlayers (correlated across all peaks with a prior of  $1\sigma$ ), and  $\mu$  is the mean error that remains. This  $\chi^2$  function is minimized with respect to  $\mu$  and  $\delta_{DL}$  and the profile likelihood is used to compute the uncertainty on  $\mu$ , using MINUIT[3]. The systematic error is taken to be

$$\sigma_{sim}^2 = \mu^2 + \sigma_{\mu}^2 \quad (1.5)$$

Tables 1.2 and 1.3 list the peak height ratios and uncertainties for each peak for module 1 and module 2, respectively. The final fractional uncertainties measured are  $\sigma_{sim,M1} = 0.0020$  and  $\sigma_{sim,M2} = 0.0047$ . This uncertainty is applied directly to the detection efficiency measured before applying any other effects such as dead layers, dead times and cuts, without any scaling. This uncertainty is one of the dominant uncertainties on the detection efficiency along with the dead layer uncertainty; while the absolute uncertainty is small, because it is applied to the detection efficiency, which tends to be  $\sim 5\%$ , directly rather than to the loss from an individual effect, the fractional uncertainty is on the order of 10%. In cases where the detection efficiency is very low, such as the 1216 keV peak in module 2 from decays to the  $2_2^+$  state, this uncertainty can completely overwhelm the detection efficiency. Figure 1.6 plots the peak height ratios for simulated and measured data for both modules 1 and 2.

### 1.3 Region of Interest Selection

Once the multisite events have been collected, we want to search for detector hits with the energies of the  $\gamma$ s emitted in each  $\beta\beta$  E.S. decay mode. To do this, a signal region of interest (ROI) must be identified. To estimate the number of background events in the signal ROI, a background ROI must also be selected near the signal ROI. This section will describe the selection of the signal and background ROIs and the calculation of the efficiency and uncertainties on the efficiency due to the ROI selection.

The peakshape function and parameters are described in Appendix ???. For each dataset, a simultaneous fit of many peaks is performed to a combined spectrum of all detectors and all calibration runs, ensuring that any variation in gain or energy nonlinearity between detectors

Table 1.2: Table of measured peak height ratios between multiplicity 1 events and multiplicity 2 events containing a 511 keV annihilation  $\gamma$  in module 1 for both simulated and measured  $^{56}\text{Co}$  spectra, with uncertainties. A plot of these numbers is shown in Figure 1.6

Peak	$\frac{A_{m2,dat}}{A_{m1,dat}}$	$\frac{A_{m2,sim}}{A_{m1,sim}}$	$\frac{A_{m2,noDL}}{A_{m1,noDL}}$	$\sigma_{dat,stat}$	$\sigma_{sim,stat}$	$\sigma_{sim,DL}$	Residual	$\sigma_{resid}$
1504 keV (SEP)	0.098	0.084	0.110	0.004	0.003	0.004	0.014	0.004
1524 keV (SEP)	0.089	0.082	0.109	0.002	0.001	0.005	0.007	0.002
2088 keV (SEP)	0.077	0.073	0.098	0.001	0.001	0.004	0.004	0.001
2499 keV (SEP)	0.081	0.079	0.108	0.003	0.002	0.005	0.002	0.004
2691 keV (SEP)	0.078	0.072	0.099	0.001	0.001	0.005	0.006	0.002
2743 keV (SEP)	0.075	0.073	0.101	0.001	0.001	0.005	0.003	0.001
2762 keV (SEP)	0.070	0.070	0.096	0.001	0.001	0.004	0.000	0.002
2940 keV (SEP)	0.075	0.070	0.100	0.002	0.002	0.005	0.005	0.003
749 keV (DEP)	0.153	0.155	0.225	0.004	0.003	0.012	-0.002	0.005
1013 keV (DEP)	0.166	0.156	0.229	0.005	0.004	0.012	0.010	0.006
1577 keV (DEP)	0.167	0.157	0.224	0.001	0.001	0.011	0.010	0.002
1988 keV (DEP)	0.158	0.155	0.222	0.005	0.005	0.011	0.003	0.007
2180 keV (DEP)	0.163	0.158	0.225	0.002	0.002	0.011	0.005	0.003
2232 keV (DEP)	0.164	0.158	0.225	0.001	0.001	0.012	0.007	0.002
2251 keV (DEP)	0.170	0.166	0.233	0.004	0.003	0.011	0.004	0.005
2429 keV (DEP)	0.165	0.158	0.230	0.005	0.004	0.012	0.007	0.007

Table 1.3: Table of measured peak height ratios between multiplicity 1 events and multiplicity 2 events containing a 511 keV annihilation  $\gamma$  in module 2 for both simulated and measured  $^{56}\text{Co}$  spectra, with uncertainties. A plot of these numbers is shown in Figure 1.6

Peak	$\frac{A_{m2,dat}}{A_{m1,dat}}$	$\frac{A_{m2,sim}}{A_{m1,sim}}$	$\frac{A_{m2,noDL}}{A_{m1,noDL}}$	$\sigma_{dat,stat}$	$\sigma_{sim,stat}$	$\sigma_{sim,DL}$	Residual	$\sigma_{resid}$
1504 keV (SEP)	0.077	0.059	0.082	0.004	0.002	0.004	0.018	0.004
1524 keV (SEP)	0.068	0.060	0.081	0.002	0.001	0.004	0.009	0.002
2088 keV (SEP)	0.059	0.054	0.074	0.001	0.000	0.003	0.005	0.001
2499 keV (SEP)	0.062	0.051	0.073	0.002	0.002	0.004	0.011	0.003
2691 keV (SEP)	0.057	0.052	0.074	0.001	0.001	0.004	0.005	0.002
2743 keV (SEP)	0.057	0.053	0.075	0.001	0.001	0.004	0.004	0.001
2762 keV (SEP)	0.055	0.050	0.071	0.002	0.001	0.004	0.005	0.002
2940 keV (SEP)	0.060	0.052	0.072	0.002	0.002	0.003	0.008	0.003
749 keV (DEP)	0.111	0.113	0.155	0.003	0.003	0.007	-0.002	0.004
1013 keV (DEP)	0.118	0.108	0.156	0.003	0.003	0.008	0.009	0.004
1577 keV (DEP)	0.119	0.113	0.161	0.001	0.001	0.008	0.006	0.001
1988 keV (DEP)	0.123	0.112	0.153	0.005	0.003	0.007	0.011	0.006
2180 keV (DEP)	0.119	0.114	0.164	0.002	0.002	0.008	0.005	0.002
2232 keV (DEP)	0.120	0.112	0.160	0.001	0.001	0.008	0.008	0.001
2251 keV (DEP)	0.124	0.120	0.170	0.003	0.003	0.008	0.004	0.004
2429 keV (DEP)	0.125	0.120	0.159	0.005	0.003	0.007	0.005	0.006

is accounted for. From each fit result, a set of parameters describing a single peak shape at the energy of the signal ROI can be extracted, along with a covariance matrix for those parameters. From these fit results, we can compute the optimal ROI, detection efficiency and uncertainty for each data set. An example of a calibration spectrum with the FWHM curve fit to it is shown in Figure 1.7.

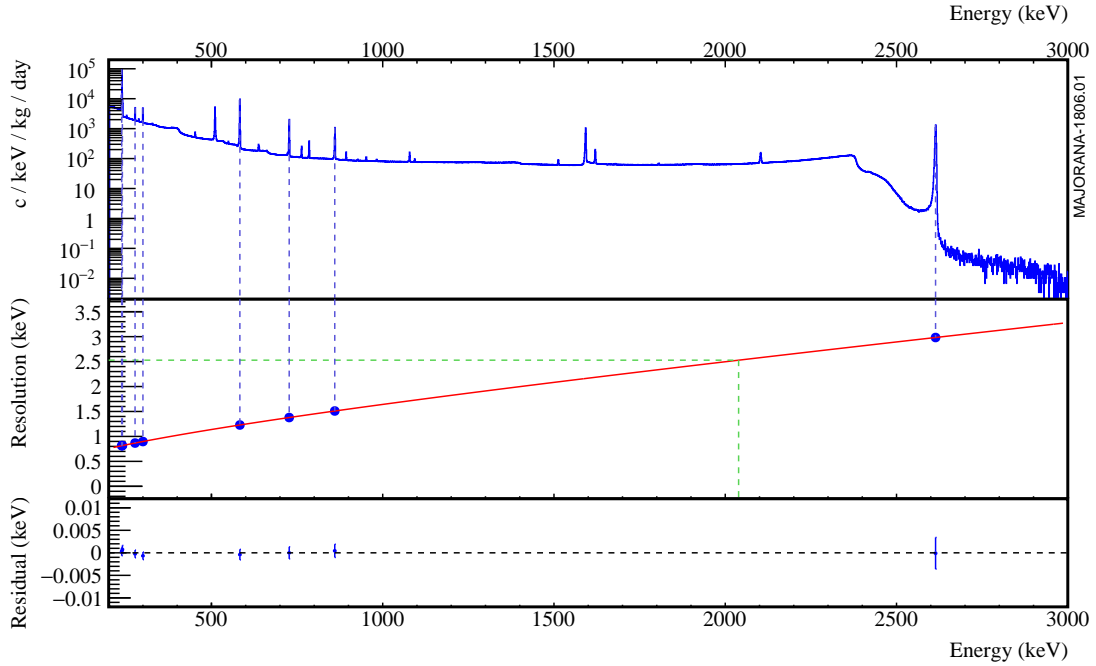


Figure 1.7: A  $^{228}\text{Th}$  calibration run with the FWHM fit curve and individual uncertainties at several peaks. This curve is used to compute the FWHM for a peak at a given energy. The statistical uncertainties are extracted from the fit result. An additional systematic uncertainty is added to account for the residuals.

### 1.3.1 Signal ROI Optimization

The signal region of interest around each peak is optimized based on the peak shape functions as fit for each data set. The optimization follows the procedure laid out in Appendix ?? and maximizes the rate sensitivity with respect to the region of interest upper and lower



boundaries,  $E_{low}$  and  $E_{high}$  respectively:

$$\hat{\Gamma}(E_{low}, E_{high}, \bar{B}) \propto \frac{DP(\bar{B}(E_{high} - E_{low}))}{\epsilon_{ROI}(E_{low}, E_{high})} \quad (1.6)$$

where DP is the discovery potential as defined in Appendix ??, and a flat background with background index  $\bar{B}$  measured from data is assumed. The efficiency is defined by the CDF of the Gaussian and LE tail components

$$\begin{aligned} \epsilon_{ROI}(E_{low}, E_{high}; \mu, \sigma, f_{tail}, \tau) = & \frac{1}{2} \left( \text{erfc} \left( \frac{E_{low} - \mu}{\sqrt{2}\sigma} \right) - \text{erfc} \left( \frac{E_{high} - \mu}{\sqrt{2}\sigma} \right) \right) \\ & + f_{tail}\tau \left( \text{ExGaus}(E_{high}; \mu, \sigma, \tau) - \text{ExGaus}(E_{low}; \mu, \sigma, \tau) \right) \end{aligned} \quad (1.7)$$

The optimal ROI is numerically calculated by minimizing  $\frac{1}{\hat{\Gamma}(E_{low}, E_{high}, \bar{B})}$  with respect to  $E_{low}$  and  $E_{high}$  using MINUIT[3].

### 1.3.2 Background ROI Selection

For each peak, a background ROI of width 50 – 100 keV surrounding the peak is selected. The ROI is selected to avoid any known background peaks and exclude them with at least 99.9% efficiency. A 99.9% exclusion region calculated from the peakshape function is selected around the peak and removed from the background ROI.

### 1.3.3 ROI Detection Efficiency and Uncertainty

The ROI detection efficiency is calculated from the CDF defined in Equation 1.7. The covariance matrix of the peak shape parameters obtained from the fit result is used to calculate the statistical uncertainty of the efficiency. Several additional systematic effects must also be accounted for:

- **Gain drift:**  $^{228}\text{Th}$  energy calibrations are taken once per week, for 90 minutes each. In between these calibration runs, the energy calibration parameters undergo small adjustments that result in energy inaccuracies for background runs taken in between. This gain drift results in an increase in the width of the peak, which is accounted

for by adding in quadrature  $\sigma_{drift}$  to the value of  $\sigma$  obtained from the fit. This also results in the dominant systematic uncertainty on the peak width,  $\delta_{fwhm,drift}$ . The gain drift also results in a small systematic error in the measured energy of the peak  $\delta_{\mu,drift}$ . A detailed description of the measurement of this systematic effect is contained in Reference [2].

- Energy nonlinearity:** While the energy response for HPGe detectors is ostensibly linear, several factors result in small nonlinearities. Local nonlinearities that are correlated over small energy scales of arise from the response of the Gretina digitizers. While these nonlinearities are corrected for, a residual nonlinearity of  $\sim 0.1$  keV with a period of  $\sim 300$  keV remains. Global nonlinearities result from systematic uncertainties in the energy estimation. One source of global nonlinearity arises from uncertainty in the start time of the waveform, which is energy dependant. Another is a small quadratic term resulting from charge recombination. Because calibrations are performed on peaks with energies ranging from 238 keV to 2614 keV, energy shifts due to global nonlinearities are very small in this range and local energy nonlinearities dominate. At smaller and larger energies, the shifts can be as large as  $\sim 0.5$  keV in some detectors. In addition to this bias, energy nonlinearities result in an increase in  $\sigma$  as a result of the combining of peaks from different detectors with different shifts; however, since the energy calibrations include all detectors, this shift is already included in the fit result, so no action is required. Energy nonlinearities also have a significant affect on the uncertainty in the measured peak energy,  $\delta_{\mu,NL}$ , which is a dominant uncertainty. A detailed description of the measurement of each of these systematic effects is contained in Reference [2].
- Detector Crosstalk:** Because we are searching for peaks in coincidence events, the possibility for a distortion in the energy measurement due to crosstalk between the involved events exists. This effect is measured in Section 1.3.4 to be small enough that no energy correction or peakshape correction is required. However, this effect does contribute to small uncertainties in the peak position,  $\delta_{\mu,xtalk}$  and peak width,

$\delta_{fwhm,xtalk}$ .

Once these uncertainties have been measured, they must be propagated into the detection efficiency. The statistical and systematic uncertainties on  $\mu$  and the FWHM are added in quadrature to obtain  $\delta_\mu$  and  $\delta_{fwhm}$ . The uncertainty on the FWHM is used to calculate a width scale uncertainty,  $\delta_\alpha$ , which is simply the fractional uncertainty on the FWHM. To compute the uncertainty on the efficiency, the efficiency is computed after modifying the peakshape parameters by one-sigma in either direction. For the uncertainty from the width, we take:

$$\begin{aligned} \sigma_{\epsilon_{ROI},fwhm} = \frac{1}{2} & \left( \epsilon_{ROI}(E_{low}, E_{high}; \mu, \sigma(1 + \delta_\alpha), f_{LE}, \tau(1 + \delta_\alpha)) \right. \\ & \left. - \epsilon_{ROI}(E_{low}, E_{high}; \mu, \sigma(1 - \delta_\alpha), f_{LE}, \tau(1 - \delta_\alpha)) \right) \end{aligned} \quad (1.8)$$

Because the ROI is optimized around  $\mu$ , shifts in the peak in either direction will cause a reduction in efficiency. For this reason, we must perform a second order propagation of uncertainties with respect to  $\delta_\mu$ . The result is a slight degradation in the efficiency, so that

$$\epsilon_{ROI} = \frac{\epsilon_{ROI}(E_{low}, E_{high}; \mu + \delta_\mu, \sigma, f_{LE}, \tau) + \epsilon_{ROI}(E_{low}, E_{high}; \mu - \delta_\mu, \sigma, f_{LE}, \tau)}{2} \quad (1.9)$$

and

$$\sigma_{\epsilon_{ROI},\mu} = \epsilon_{ROI}(E_{low}, E_{high}; \mu, \sigma, f_{LE}, \tau) - \epsilon_{ROI} \quad (1.10)$$

These uncertainties are taken to be uncorrelated and added in quadrature to obtain the final uncertainty on the ROI efficiency. Table 1.4 contains a full summary of all of the energy uncertainties, the ROIs, and the ROI efficiencies and uncertainties.

#### 1.3.4 Detector Crosstalk

Detector crosstalk is caused when a true signal in one detector channel induces a small signal in another channel. This is not a large enough effect to trigger events in a separate channel, meaning that it does not effect single-detector events. However, it could produce an energy estimation error in multi-detector events since coincident pulses could induce signals that interfere either constructively or destructively, shifting the measured energies. In practice,

Table 1.4: Table of energy estimation uncertainties, regions of interest, and efficiencies

DS	$E_{peak}$ (keV)	$\sigma_{fit}$ (keV)	$\sigma_{drift}$ (keV)	$\sigma$ (keV)	$f_{s,fit}$	$\tau_{fit}$ (keV)	$\delta_{\mu,fit}$ (keV)	$\delta_{\mu,NL}$ (keV)	$\delta_{\mu,drift}$ (keV)	$\delta_{\mu,stack}$ (keV)	$\delta_{\mu,peak}$ (keV)	$\delta_{\mu}$ (keV)	FWHM (keV)	$\delta_{fwhm,fit}$ (keV)	$\delta_{fwhm,drift}$ (keV)	$\delta_{fwhm,stack}$ (keV)	$\delta_{fwhm}$ (keV)	$\delta_{\alpha}$	$E_{ROI,1}$ (keV)	$E_{ROI,2}$ (keV)	$\epsilon_{ROI}$	$\sigma_{ROI}$
DS1	559.101	0.460	0.063	0.464	0.230	0.515	0.001	0.104	0.002	0.012	0.005	0.105	1.152	0.001	0.039	0.011	0.040	0.035	558.199	559.847	0.871	0.015
DS2	559.101	0.461	0.055	0.464	0.249	0.515	0.002	0.067	0.004	0.012	0.005	0.068	1.158	0.001	0.107	0.011	0.108	0.063	558.186	559.845	0.874	0.031
DS3	559.101	0.470	0.066	0.474	0.224	0.505	0.001	0.026	0.024	0.012	0.005	0.038	1.174	0.001	0.073	0.011	0.074	0.063	558.187	559.863	0.879	0.021
DS4	559.101	0.455	0.077	0.461	0.108	0.445	0.002	0.076	0.010	0.012	0.005	0.078	1.111	0.001	0.106	0.011	0.107	0.096	558.283	559.856	0.888	0.032
DS5a	559.101	0.560	0.085	0.567	0.106	0.855	0.002	0.079	0.005	0.012	0.005	0.080	1.367	0.002	0.055	0.011	0.056	0.041	558.098	560.022	0.875	0.014
DS5b	559.101	0.469	0.074	0.475	0.158	0.491	0.001	0.020	0.011	0.012	0.005	0.026	1.157	0.001	0.125	0.011	0.125	0.108	558.229	559.872	0.885	0.036
DS5c	559.101	0.460	0.085	0.468	0.174	0.489	0.001	0.037	0.030	0.012	0.005	0.050	1.145	0.001	0.162	0.011	0.162	0.142	558.231	559.860	0.883	0.046
DS6a	559.101	0.456	0.044	0.458	0.191	0.463	0.001	0.069	0.025	0.012	0.005	0.075	1.123	0.000	0.041	0.011	0.042	0.038	558.241	559.841	0.881	0.014
DS1	563.178	0.461	0.064	0.466	0.230	0.518	0.001	0.104	0.002	0.012	0.005	0.105	1.156	0.001	0.039	0.011	0.040	0.035	562.273	563.927	0.871	0.015
DS2	563.178	0.463	0.055	0.466	0.249	0.517	0.002	0.067	0.004	0.012	0.005	0.068	1.162	0.001	0.107	0.011	0.108	0.093	562.259	563.924	0.874	0.030
DS3	563.178	0.471	0.066	0.476	0.224	0.508	0.001	0.026	0.024	0.012	0.005	0.038	1.179	0.001	0.073	0.011	0.074	0.063	562.261	563.943	0.879	0.021
DS4	563.178	0.457	0.077	0.463	0.108	0.447	0.002	0.076	0.010	0.012	0.005	0.078	1.115	0.001	0.106	0.011	0.107	0.096	562.357	563.935	0.888	0.032
DS5a	563.178	0.562	0.086	0.569	0.106	0.858	0.002	0.079	0.006	0.012	0.005	0.080	1.372	0.002	0.055	0.011	0.056	0.041	562.172	564.103	0.875	0.014
DS5b	563.178	0.471	0.074	0.477	0.158	0.494	0.001	0.020	0.011	0.012	0.005	0.026	1.162	0.001	0.125	0.011	0.125	0.108	562.303	563.952	0.885	0.035
DS5c	563.178	0.462	0.086	0.470	0.174	0.492	0.001	0.037	0.030	0.012	0.005	0.050	1.149	0.001	0.162	0.011	0.162	0.141	562.305	563.939	0.883	0.046
DS6a	563.178	0.457	0.044	0.459	0.191	0.465	0.001	0.069	0.026	0.012	0.005	0.075	1.127	0.000	0.041	0.011	0.042	0.038	562.315	563.921	0.881	0.013

this could produce both a shift and additional uncertainty in both the measured energy of the peak and in the width of the peak. To check for this effect, we can look at multi-detector events in  $^{228}\text{Th}$  calibration data. In particular, we will compare the centroid and FWHM for several peaks in both single-detector events and multi-detector events.

5 peaks were selected from the  $^{208}\text{Tl}$   $\gamma$  cascade, at 277, 583, 763, 860 and 2614 keV, and one additional peak was selected from the  $^{212}\text{Bi}$  cascade, at 785 keV. These peaks were selected based on their prominence in the high multiplicity hit spectrum. The combined calibration spectra from dataset 6 were used to perform this analysis. These peaks were fit individually, and the centroid and FWHM were computed for multiplicity 1 and multiplicity 2 events. Figure 1.8 shows the results of these measurements. While a very small reduction in peak centroid and increase in peak width are observed, the shifts are small compared to the existing uncertainties in these parameters. As a result, we will ignore this shift and instead compute an uncertainty in each parameter caused by crosstalk. We will treat the systematic error as uncorrelated between the peaks and compute the necessary error needed to make the combined statistical and systematic errors large enough to make the  $\chi^2$  value computed by comparing these peaks equal to 1:

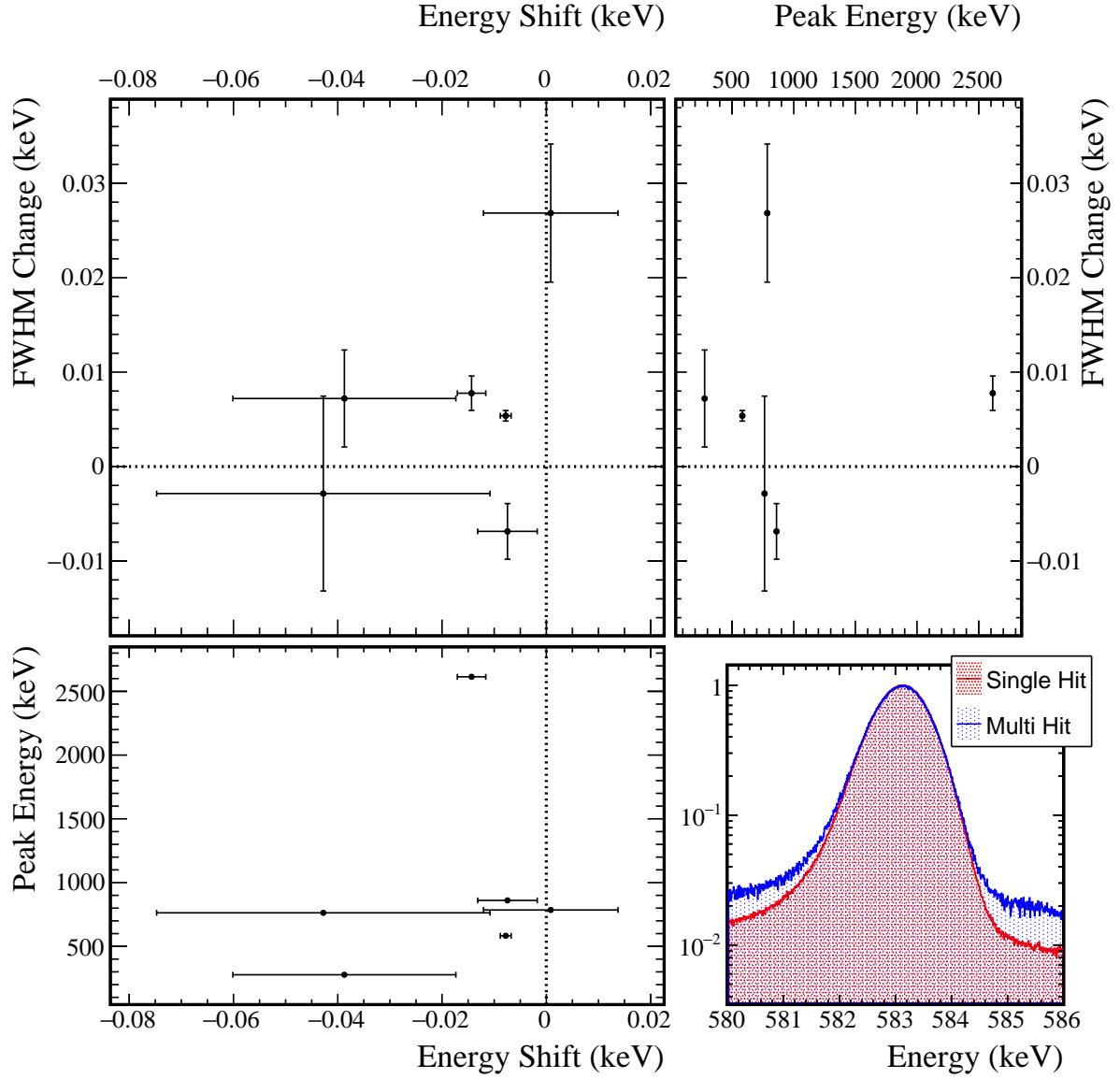
$$\chi^2 = \sum_{k=0}^N \frac{(\text{cen}_{k,m1} - \text{cen}_{k,m2})^2}{\sigma_{\text{cen},k,m1}^2 + \sigma_{\text{cen},k,m2}^2 + \delta_{\mu,\text{xtalk}}^2} \quad (1.11)$$

$$\chi^2 = \sum_{k=0}^N \frac{(\text{FWHM}_{k,m1} - \text{FWHM}_{k,m2})^2}{\sigma_{\text{fwhm},k,m1}^2 + \sigma_{\text{fwhm},k,m2}^2 + \delta_{\text{fwhm},\text{xtalk}}^2} \quad (1.12)$$

Both systematic errors are numerically computed using a Brent minimization algorithm. The results are  $\delta_{\mu,\text{xtalk}} = 0.012$  keV and  $\delta_{\text{fwhm},\text{xtalk}} = 0.011$  keV, both of which are subdominant uncertainties.

#### 1.4 Background Cuts

By making use of known properties of background events, data cleaning cuts can be designed to selectively reduce backgrounds while minimizing sacrifice of excited state events. Because



(a) Module 1

Figure 1.8: Difference of the measured centroid and FWHM of several  $^{228}\text{Th}$  calibration peaks. Error bars represent the fit errors. Notice on the bottom right, that any difference is not visible to the naked eye.

of the multi-detector event nature of the event selection, many of these background cuts are designed to make use of observables from the detector hits in coincidence with candidate hits.

#### 1.4.1 Enriched Source Detector Cut

Since the  $\beta\beta$  E.S. events must originate in  $^{76}\text{Ge}$ , events are far likelier to originate in enriched HPGe detectors than those with natural germanium isotopic abundances. There are 29.8 kg of enriched detectors, with  $88.1 \pm 0.7\%$  abundance of  $^{76}\text{Ge}$  and 14.4 kg of natural detectors, with  $7.83 \pm 0.07\%$  abundance of  $^{76}\text{Ge}$ . This means that  $95.8 \pm 0.1\%$  of  $\beta\beta$  E.S. events will originate in enriched detectors. If we assume that background events will hit all detector mass at the same rate, then we would expect only 67% of hits from background events involving two detectors to be in coincidence with a hit in an enriched detector. This means that a significant gain in sensitivity can be achieved by cutting hits that are not in coincidence with an enriched detector hit. While the detection efficiency of this cut is expected to be close to 95.8%, the actual efficiency is measured from simulations, and tends to be greater, since a greater proportion of enriched detectors are active compared to natural detectors.



Figure 1.9: Diagram showing each detector in each module, arranged by which string and position they are in. Enriched detectors are colored green and natural detectors are colored blue. 95% of  $^{76}\text{Ge}$  in the array is contained in the enriched detectors.

### 1.4.2 Coincident and Sum Energy Cuts

The greatest source of background events is expected to be  $\gamma$ -rays from a handful of known primordial and cosmogenic isotopes. Because  $\gamma$ -rays are monoenergetic, they will often present a clear detection signature that can be targeted.  $\gamma$ -rays will often Compton scatter from one detector into another, depositing their entire energy between the two. For this reason, events whose total energy is equal to the energy of a known  $\gamma$  can be cut.  $\beta$ -decays will often result in a cascade of multiple  $\gamma$ s, at least one of which may be fully absorbed in a single detector. These events can be cut by searching for a coincident detector with energy equal to that of a known  $\gamma$ . Finally, whereas the  $\beta\beta$  decay spectrum approaches zero amplitude at low energies and at  $Q_{\beta\beta}$ , the Compton continuum of  $\gamma$ s has a large amplitude at low energies. This means that sensitivity can be gained by setting low- and high-energy thresholds on hits in coincidence with a candidate event. These combined backgrounds can be reduced by cutting events with either sum energies or coincident hit energies that fall in a set of energy ranges. For  $\beta\beta$  E.S. modes with multiple  $\gamma$ s, the optimal energy ranges will differ between natural and enriched detectors, since natural detectors will mostly include hits from one of the  $\gamma$ s, while enriched events will include  $\beta\beta$  hits,  $\gamma$  hits, and pileup events including both of these, allowing a much wider energy range. For this reason, a separate set of coincident cut energy ranges are used for natural and enriched detectors.

The energy ranges that are cut can be determined by comparing the background model simulation to simulations of each  $\beta\beta$  E.S. decay mode. An algorithm was written that simultaneously selects a set of both sum and coincident energy ranges to cut that optimizes discovery potential, as defined in Appendix ?? . The algorithm begins by identifying events in the  $\beta\beta$  E.S. simulation that include at least one hit consisting of the full absorption of a  $\gamma$  photon and events in the background model simulation that include at least one hit in the background region of interest. These events are then sorted into energy bins for each coincident hit and for the sum energy of the event (a single event will be in multiple bins). For each bin, the algorithm checks the change in discovery potential if the bin was toggled to



be either cut or included. Following Equation ??, the discovery potential will be improved by toggling bin  $k$  if:

$$\text{DP}'(s \cdot N_{BG}) \frac{s \cdot n_{k,BG}}{\text{DP}(s \cdot N_{BG})} < \frac{n_{k,ES}}{N_{ES}} \quad (1.13)$$

where  $N_{ES}$  and  $N_{BG}$  are the total number of events remaining in the simulated  $\beta\beta$  E.S. and background spectra, respectively;  $s$  is a scaling to estimate the number of background events in the data from the number in the simulation; and  $n_{k,ES}$  and  $n_{k,BG}$  are the number of simulated  $\beta\beta$  E.S. and background events contained in the bin. A  $\chi$  value is computed representing the normal quantile of the probability that cutting or including the bin will improve the discovery potential. This is done by assuming that the uncertainty on the number of events in the bin is Gaussian distributed, with standard deviations  $\sqrt{n_{k,ES}}$  and  $\sqrt{n_{k,BG}}$ , respectively. In this case, we get:

$$\chi_k = \frac{\frac{n_{k,ES}}{N_{ES}} - \text{DP}'(s \cdot N_{BG}) \frac{s \cdot n_{k,BG}}{\text{DP}(s \cdot N_{BG})}}{\sqrt{\left(\text{DP}'(s \cdot N_{BG}) \frac{s}{\text{DP}(s \cdot N_{BG})}\right)^2 n_{k,BG} + \frac{n_{k,ES}}{N_{ES}^2}}} \quad (1.14)$$

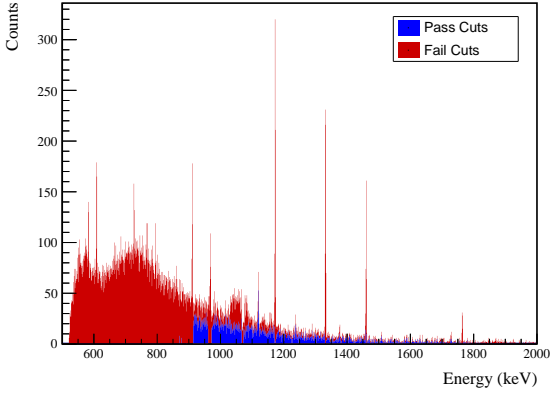
All events in the bin with highest probability of improving the discovery potential are then either cut or included, and must be cut or included to all other bins that they fall into. Note that a included event will only be included if it is not cut by any other bin. This process is repeated until toggling any bin will have  $\chi_k < 0$ , meaning there is a  $< 50\%$  chance of improving the discovery potential. At this point, the bins are then combined in order to determine the ranges of energies to be cut in sum energy and coincident energies.

Because of limited statistics in the simulations, this cut will be biased to cut events in bins with a downward fluctuation in  $\beta\beta$  E.S. rate and accept bins with an upward fluctuation, and vice-versa for the simulated background model. In order to minimize this bias and ensure that energy ranges are selected based on real backgrounds rather than statistical fluctuations, a penalty is applied to the probability calculations if a new range would be added. If a cutting or readding a bin would increase the number of energy ranges, a penalty of 3 is added to the  $\chi$  value, and if it would reduce the number of ranges, a penalty of -3 is added. This corresponds to requiring a 99.8% chance that adding a new energy range will

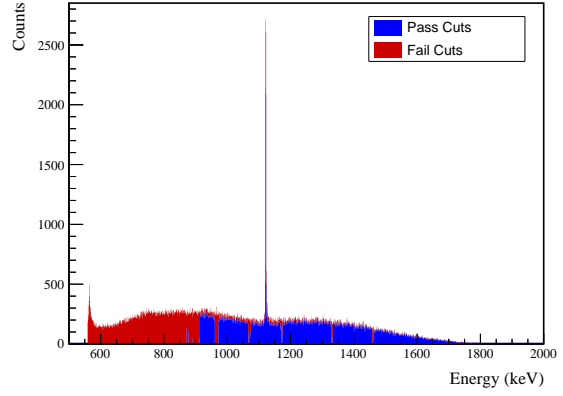
represent an improvement before we conclude that it is not a statistical fluctuation. This is inspired by the Akaike Information Criterion (AIC)[1], which adds a penalty of 1 to a likelihood for each parameter added to a model. In this case, adding an energy range adds two parameters to our cut, so the equivalent penalty is 1.5 per parameter, which is a larger penalty than AIC. This difference can be explained by the fact that the AIC penalty of 1 requires 97.7% that toggling a bin represents an improvement; however, it has been observed that  $\sim 100$  bins exist close enough to the threshold for inclusion or exclusion to accidentally toggle the bin. As a result, using a penalty of 1 will result in multiple accidentally excluded energy regions, on average, while a penalty of 1.5 will not.

To further control limited simulation statistics, a variety of bin widths is used to determine the optimal energy ranges. This is necessary because with a narrow binning, bins do not have enough statistics to overcome the penalty described above, but wider bins produce very imprecise energy ranges. The algorithm starts by optimizing the cut ranges with a bin width of 6.4 keV starting from a prior of cutting no energy ranges. Once this optimization is complete, the bin width is split in half and the algorithm re-optimizes the energy ranges, using the previous ranges as a prior. This halving of bin width is repeated until a final bin width of 0.2 keV is reached. The results of this cut optimization procedure are shown in figures 1.10 and 1.11.

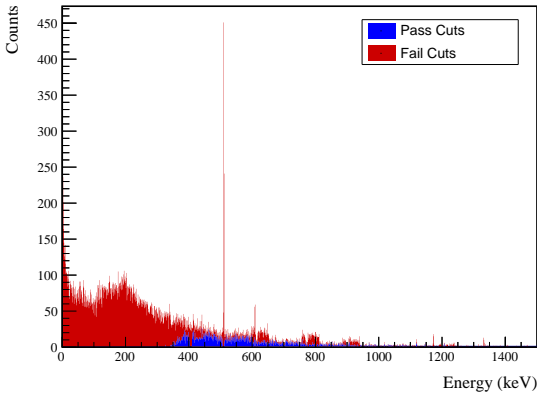
The efficiency of each of the sum and coincident energy cuts can be evaluated by computing the ratio of simulated  $\beta\beta$  E.S. events that pass the cut to the total number of simulated events. The primary source of uncertainty arises from imperfections in the simulated  $\beta\beta$  E.S. spectra produced by DECAY0 (see Section ??). Additionally uncertainty in the spectral shape arises from energy nonlinearity. Since the efficiency is calculated by integrating over portions of the coincidence spectrum, an upper limit on the systematic error can be found using the KS statistic of a comparison between the simulated spectrum and the true spectrum. As discussed in Section ??, we can perform this comparison by using the Kotila and Iachello spectrum as a proxy. This relies on the assumption that the Kotila and Iachello spectrum has corrected the dominant errors in the DECAY0 spectrum; if any errors coexist in both



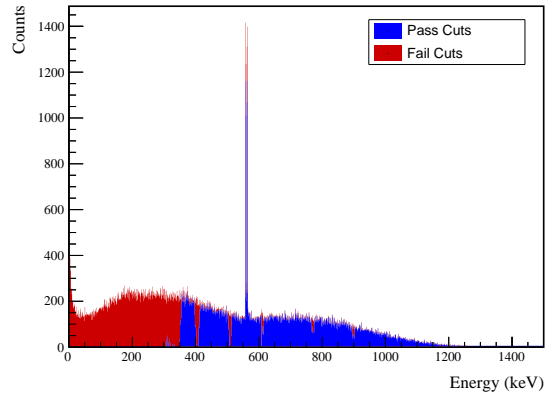
(a) Simulated BG Sum Energy Spectrum



(b) Simulated ES Sum Energy Spectrum



(c) Simulated BG Coincident Energy Spectrum



(d) Simulated ES Coincident Energy Spectrum

Figure 1.10: Top: Simulated sum energy spectra of simulated ES and BG events. The events in red are cut by the sum- or coincident-energy cut. Note that regions around many peaks are cut, as intended.

Bottom: Simulated energy spectrum of events in coincidence with events in the ROI. Excesses in red are cut by the sum- or coincident-energy cut. Once again, regions around prominent peaks are cut out as intended.

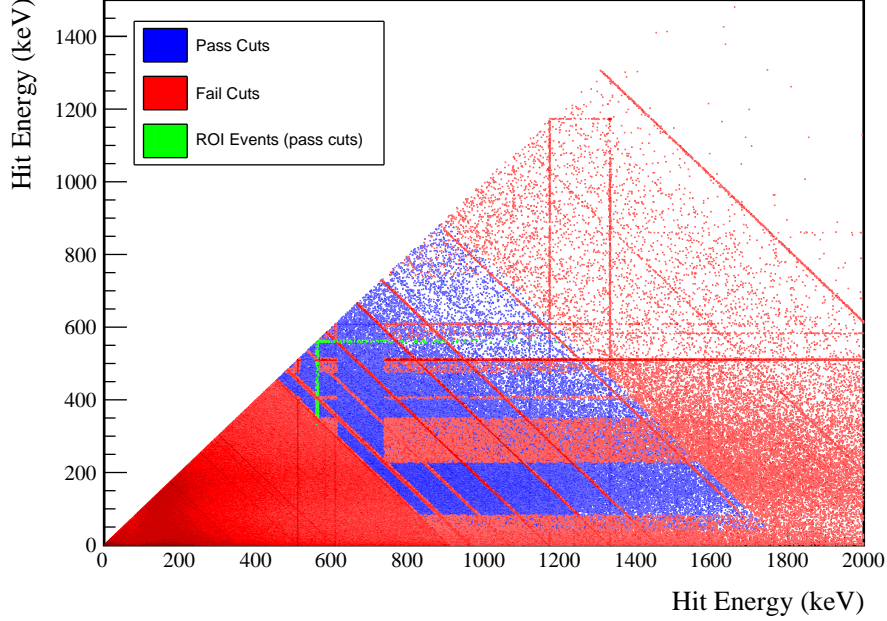


Figure 1.11: 2D energy spectrum of simulated BG events. Blue bins have at least one hit that passes both the sum- or coincident-energy cuts. For red bins, both hits have failed at least one of these cuts. Green bins have at least one hit in the BG or ES ROI that passes these cuts.

spectra that have a similar order of magnitude, then this approach will underestimate the uncertainty. To account for energy nonlinearity, each simulated energy is shifted to represent the effects of digitizer nonlinearity and energy drift. Digitizer nonlinearity originates from the fact that some digitizer energy bins are slightly wider than others and has an approximately sawtooth dependency on energy with a period of  $\sim 600$  keV. A correction is applied that reduces the size of this nonlinearity to  $\sim 0.1$  keV in magnitude and smooths it out significantly, as shown in Figure 1.12. Digitizer nonlinearity is included in the simulation by shifting each energy according to a sawtooth function with rms 0.1 keV and period 600 keV:

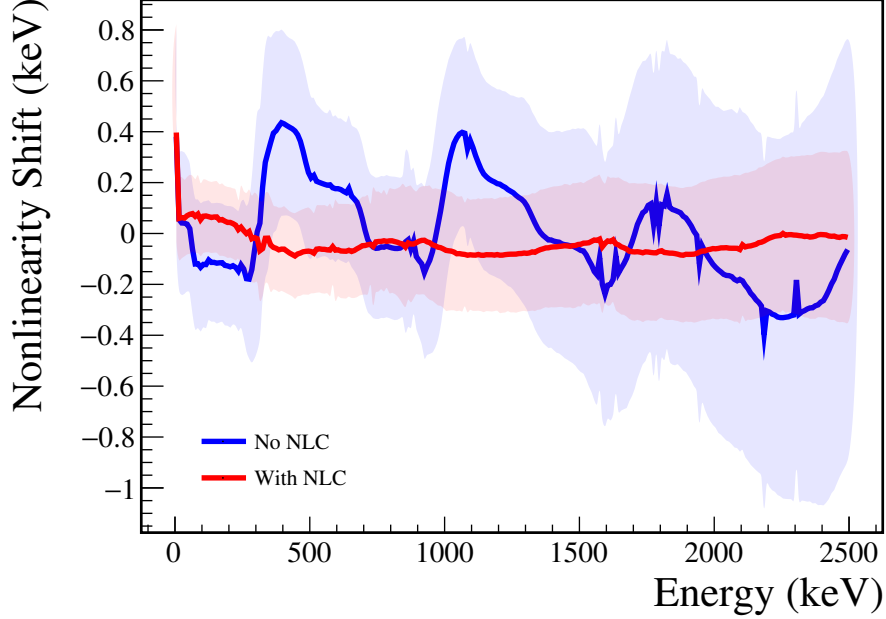


Figure 1.12: Digitizer nonlinearity before (red) and after (blue) being corrected. This nonlinearity is measured by comparing the energy measured in the high gain channel to that of the low gain channel.

$$\Delta(E) = \sqrt{3} \cdot (0.1 \text{ keV}) \left( \text{rem} \left( \frac{E - 150 \text{ keV}}{600 \text{ keV}} \right) \right) \quad (1.15)$$

where `rem` is the remainder function as defined in the C++ standard library. An additional shift that is randomly sampled from a Gaussian distribution with standard deviation  $0.00015 \cdot E$  is applied to simulate the effect of gain drift, based on the drift observed during DS5. After applying both of these alterations to the `decay0` spectrum, a KS test is performed against the Kotila and Iachello spectrum, and a maximum CDF difference of 0.08% is observed, as shown in Figure 1.13. This difference is used as an upper limit on the uncertainty from the energy range cuts for  $2\nu\beta\beta$  modes.

For  $0\nu\beta\beta$ , the energy ranges selected by this cut surround peaks corresponding to the

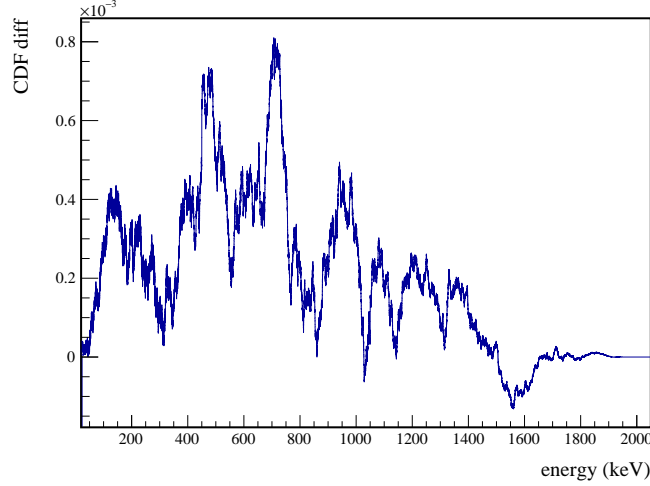


Figure 1.13: KS test comparing the CDFs of the simulated DECAY0  $2\nu\beta\beta$  ground state decay with energy nonlinearity modifications applied to the Kotila and Iachello simulated spectrum.

$Q_{\beta\beta}$ s of the decay modes or sum peaks of the  $Q_{\beta\beta}$  with a deexcitation  $\gamma$ . In this case, since we are no longer integrating over a  $\beta\beta$ -spectrum, the uncertainty in the efficiency will depend on shifts in the peak, similar to the ROI-efficiency. Since the energy regions selected keep at least 99.9% of these peaks in all cases, we can set an upper limit on the uncertainty by checking the ROI efficiency uncertainty around the 2039 keV  $Q_{\beta\beta}$ , assuming an ROI tuned to select 99.9% of the peak. The uncertainty observed in this case is 0.325%, which is applied to the energy range cuts for  $0\nu\beta\beta$  modes. For both  $0\nu\beta\beta$  and  $2\nu\beta\beta$  modes, this efficiency uncertainty is sub-dominant, so these highly conservative uncertainty estimates will suffice.

#### 1.4.3 Muon Veto Cut

Cosmic ray muons have the potential to produce partial showers in the MAJORANA DEMONSTRATOR that can produce multi-site event events and can activate short-lived isotopes that in turn may decay, producing delayed multi-site event events. Background events caused

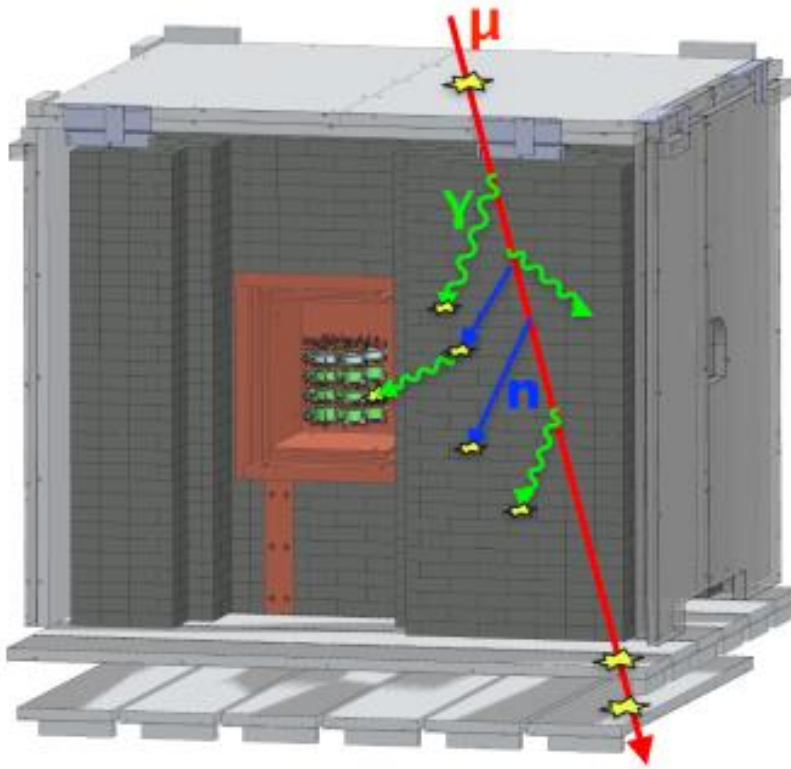


Figure 1.14: A cartoon of a particle shower created by a muon event. The particles produced in such a shower can hit multiple detectors, producing multi-detector events.

by muons can be cut using the muon veto system described in Section ?? . This analysis follows the standard MAJORANA DEMONSTRATOR muon cut procedure, for which any HPGe detector events occurring 20 ms before and 1 s after a tagged muon event are cut. This cut will remove  $> 99.9\%$  of events induced by the muon shower, based on simulations[5]. In reality, the cut efficiency is slightly lower due to periods of time where the muon veto system clock became desynchronized with the Germanium detector clock. The impact of this cut is to reduce the total livetime in each module by  $< 40$  s per day[5].

### 1.5 Combined Detection Efficiency for $\beta\beta$ E.S.

The final efficiency measurement combining all of the effects described in this chapter for each  $\beta\beta$  E.S. mode is measured directly from the simulations by computing the ratio of events that survive all cuts and effects to the total number of generated events. The efficiency used is the exposure-weighted average of the simulated efficiency for each subdataset. Because each module is an independent measurement, separate efficiencies are measured for modules 1 and 2. Because of correlations causing the probability of certain effects causing sacrifice of a  $\beta\beta$  E.S. event to be conditional on other effects, the combined efficiency will differ from simply being the product of the individual efficiencies. This means that the combined efficiency  $\epsilon_{comb}$  for each effect  $k$  is:

$$\epsilon_{comb} = \prod_{k=0}^N P(\text{event is cut} | \text{cuts } 0 \dots k-1 \text{ are applied}) \quad (1.16)$$

In spite of this, we will assume that the sources of error are uncorrelated and the fractional uncertainty is independent of what other effects have been applied. The effect of this assumption will be discussed below. This implies that the uncertainty on the combined efficiency,  $\sigma_{\epsilon,comb}$  can be expressed as:

$$\sigma_{\epsilon,comb} = \epsilon_{comb} \sqrt{\sum_{k=0}^N N \left( \frac{\sigma_{\epsilon,k}}{\epsilon_k} \right)^2} \quad (1.17)$$

The values  $\epsilon_k$  represent the probability of cutting an event assuming no other analysis cuts are applied. Because of correlations among the cuts (particularly between the sum and coincident



energy cuts), this results in a double-counting of uncertainty, making this a conservative estimate.

Table 1.5 shows the efficiency for each effect described in this chapter and uncertainty on each efficiency, and the combined efficiency and uncertainty. Similar tables for each other

Source	Module 1 efficiency	Module 2 efficiency
Multi-Detector with Full Energy $\gamma$	$5.9 \pm 0.2\%$	$3.2 \pm 0.5\%$
Region of Interest	$87.9 \pm 1.4\%$	$87.9 \pm 1.4\%$
Dead Layer	$74.5 \pm 4.3\%$	$65.7 \pm 6.0\%$
Detector Dead Times	$97.5 \pm 1.2\%$	$98.1 \pm 0.9\%$
Enriched Source Detector Cut	$96.8 \pm <0.1\%$	$89.4 \pm <0.1\%$
Coincident Energy Cut	$88.5 \pm 0.5\%$	$84.4 \pm 0.5\%$
Sum Energy Cut	$60.2 \pm 0.5\%$	$54.0 \pm 0.5\%$
Final Efficiency	$2.29 \pm 0.16\%$	$0.97 \pm 0.17\%$

Table 1.5: Table of detection efficiencies and uncertainties for  $2\nu\beta\beta$  of  $^{76}\text{Ge}$  to the  $0_1^+$  state of  $^{76}\text{Se}$ . Efficiencies of individual effects are calculated without applying other cuts; because of correlations between cuts (especially the sum and coincident energy cuts), simply multiplying these efficiencies together will underestimate the efficiency. The final efficiency calculated here correctly accounts for such correlations. Note that the efficiencies are the combined efficiency for the 559 and 563 keV peaks.

$\beta\beta$  E.S. peak are shown in Appendix ???. In all cases the dominant uncertainties come from either the dead layer thickness or the simulation uncertainty. Figure 1.15 shows the effect of each cut as it is applied sequentially to the  $2\nu\beta\beta$  to  $0_1^+$  peaks.

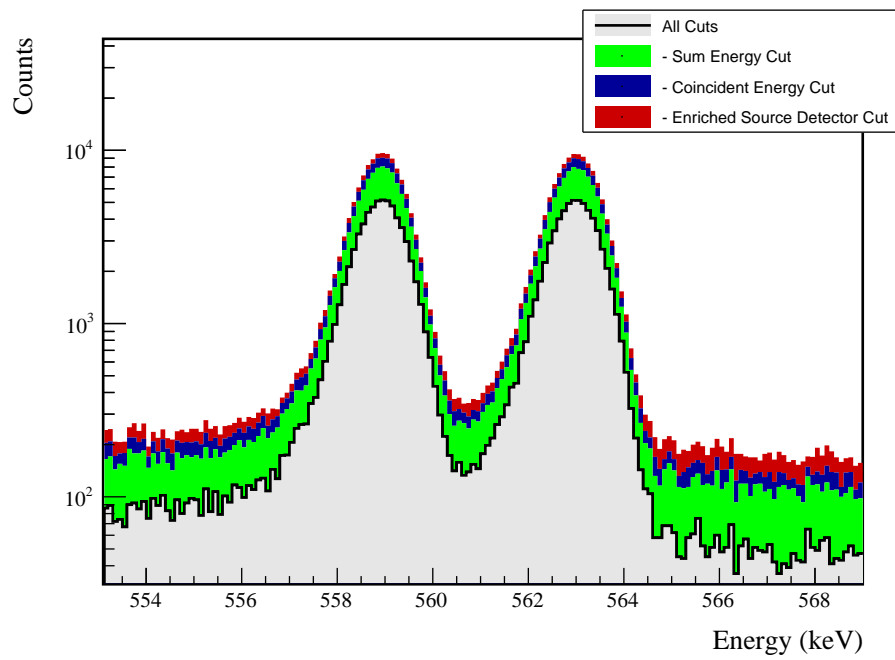


Figure 1.15: The 559 and 563 keV peaks from the  $2\nu\beta\beta$  decay to the  $0_1^+$  decay mode, with the effect of all cuts applied sequentially to simulated ES events. The cuts are applied from top to bottom (i.e. red, blue, then green). Many events will be cut by more than one of these; in that case it will be colored by whichever cut is applied first.

## BIBLIOGRAPHY

- [1] H. Akaike. A new look at the statistical model identification. *IEEE Transactions on Automatic Control*, 19(6):716–723, December 1974.
- [2] P. Chu, J. Detwiler, and I. Guinn. Energy systematic of MAJORANA DEMONSTRATOR. Technical Report 2017-021, Los Alamos National Laboratory, Oct 2017.
- [3] F. James. MINUIT Function Minimization and Error Analysis: Reference Manual Version 94.1. Technical Report CERN-D506, CERN CN Division, Geneva, 1994.
- [4] A Reine, T Caldwell, C Cuesta, I Guinn, and J Myslik. Run selection and data cleaning of ds5 (m1 and m2) (internal). Technical Report 2017-020, University of North Carolina at Chapel Hill, May 2018.
- [5] C Wiseman. Muon veto analysis for the MAJORANA DEMONSTRATOR (internal). Technical report, University of South Carolina, 2016.